Thickness-Dependent Perpendicular Magnetic Anisotropy and Gilbert Damping in $Hf/Co_{20}Fe_{60}B_{20}/MgO$ Heterostructures

James Lourembam,[*,†] Abhijit Ghosh,[†] Minggang Zeng,[‡] Seng Kai Wong,[†] Qi Jia Yap,[†] and Sze Ter Lim[†]

*Data Storage Institute, Agency for Science, Technology and Research (A*STAR), 2 Fusionopolis Way, #08-01 Innovis, Singapore 138634*

(Received 2 May 2018; revised manuscript received 22 July 2018; published 24 October 2018)

$Hf/Co_{20}Fe_{60}B_{20}/MgO$ is an attractive alternative free-layer structure for the realization of high-thermal-stability magnetoresistance random access memory (MRAM) because of its enhanced perpendicular magnetic anisotropy (PMA). Writing energy, which is equally crucial for MRAM, is determined not just by its PMA, but also by Gilbert damping and is so far unknown for this system. These parameters are particularly important in ultrathin $Co_{20}Fe_{60}B_{20}$ (t_{CFB} <1.3 nm) for implementation in MRAM. Within this short thickness range, we find that the measured damping varies dramatically from approximately 0.026 to approximately 0.012. This strong thickness-dependent damping is attributed to extrinsic spin-pumping effects as revealed by the large spin-mixing conductance of approximately 10^{20} m^{-2}. It is also found through first-principles calculations that the intrinsic damping in this system will be larger in comparison to bulk $Co_{20}Fe_{60}B_{20}$. We also establish that a previously excluded higher-order anisotropy term is crucial in the accurate determination of interfacial PMA in $Hf/Co_{20}Fe_{60}B_{20}/MgO$. Unlike similar perpendicular heterostructures, this system provides wide tunability in damping, opening up opportunities for niche applications in spintronics.

DOI: 10.1103/PhysRevApplied.10.044057

I. INTRODUCTION

Magnetic tunnel junctions (MTJ) with perpendicular magnetic anisotropy based on $Co_xFe_{80-x}B_{20}/MgO$ material systems form elementary structures for realizing high-density magnetoresistance random access memories (MRAMs) with low power consumption [1–10]. One of the extensively researched heterostructure designs for MRAM is nonmagnetic metal (NM)/$Co_xFe_{80-x}B_{20}/MgO$, which is employed as a magnetic free layer in perpendicular MTJs (PMTJs) [2,11–14]. The NM, grown sequentially as the underlayer or capping layer, is usually chosen to be a "boron-sink" material that can pull boron atoms from the amorphous $Co_xFe_{80-x}B_{20}$ film during the postdeposition annealing process [2,14]. This process results in the crystallization of bcc (001) Co-Fe, with the MgO layer acting as the crystal template, and leaving behind metal boride in the underlayer [14–16]. This epitaxy is crucial for achieving interfacial perpendicular magnetic anisotropy (PMA) and promotes coherent tunneling thereby increasing tunneling magneto-resistance (TMR) [1,2,17–19]. High thermal stability has also been reported in NM/$Co_xFe_{80-x}B_{20}/MgO$ PMTJ structures [11].

Material selection for the NM layer is critical in the optimization of the MTJ stack. Tantalum (Ta) is the most popular NM layer in the magnetic free-layer structure due to its high affinity with boron, and because it allows subsequent bcc crystallization of the adjacent $Co_xFe_{80-x}B_{20}$ layer. Several NM underlayers including Pd, Zr, Ru, W, Hf, and Mo have also been investigated with the purpose of further increasing the thermal stability and the TMR [2,12–14,20–22]. Perpendicularly magnetized NM/$Co_xFe_{80-x}B_{20}/MgO$ can also be utilized for the development of alternative ultralow power writing schemes via voltage-controlled magnetic anisotropy (VCMA) or spin-orbit torque [23–29].

Hafnium (Hf) is a suitable alternative to Ta as a boron-sink underlayer and has been demonstrated to enhance PMA in $Co_xFe_{80-x}B_{20}/MgO$ compared to Ta, Ru, W, or Pt [13]. Hence, Hf is a promising underlayer choice for producing PMTJs with higher thermal stability. However, optimization of PMTJs for MRAM requires a reduction in switching current as well as improvement in thermal stability within the same structure. The reduction in switching current is dependent on both PMA and the

*james_lourembam@imre.a-star.edu.sg

†Present address: Institute of Materials Research and Engineering, Agency for Science Technology and Research (A*STAR), #08-03, 2 Fusionopolis Way, Innovis, 138634, Singapore

‡Present address: Institute for Infocomm Research, Agency for Science Technology and Research (A*STAR), 1 Fusionopolis Way, #21-01 Connexis (South Tower), 138632, Singapore

Gilbert damping parameter, which thus far is unknown. Integration of $Hf/Co_xFe_{80-x}B_{20}/MgO$ as the free layer necessitates a comprehensive materials investigation of the system. Fundamental understanding of unexplored interfacial spin properties of the system including magnetoelastic effects, spin-scattering mechanisms, spin pumping, and spin-mixing conductance will guide engineering optimizations. In particular, in the context of free-layer development for MRAM, it is vital to explore these properties in the ultrathin limit of ferromagnet thickness, $t_{CFB} < 1.3$ nm.

In this work, we seek a comprehensive understanding of the spin properties in ultrathin $Hf/Co_{20}Fe_{60}B_{20}/MgO$ by integrating the techniques of magnetometry, ferromagnetic resonance, and first-principles calculations. PMA in the system is revisited by accounting for higher-order anisotropy terms and the role of interfacial orbitals, which addresses open questions about previously determined values of interfacial magnetic anisotropy. In addition, we present a report on damping and the associated nonlocal or extrinsic effects in magnetization dynamics such as spin pumping and two-magnon scattering. We also report the value of spin-mixing conductance, an important parameter for spin pumping at the $Hf/Co_{20}Fe_{60}B_{20}$ interface.

II. METHODS

A series of Hf-underlayer films are grown in a Singulus Timaris sputtering system, with stack configuration—substrate/seed/Hf(5)/$Co_{20}Fe_{60}B_{20}(t_{CFB})$/MgO(2)/cap. The seed layer is composed of Ta(5)/Ru(5) and SiO_2(8) is used as the capping layer. Nominal thicknesses are represented in parenthesis in nanometers (nm). Another series of films—substrate/seed/MgO(2)/$Co_{20}Fe_{60}B_{20}(t_{CFB})$/MgO(2)/cap is sputter deposited as reference materials for magnetization damping studies. Postdeposition annealing is carried out at 300 °C without breaking the vacuum.

Room-temperature magnetic moments are characterized using Micromag alternating gradient magnetometry (AGM) on samples that are diced to 3×3-mm^2-sized coupons using an Okamoto dicer (ADM-6D). Magnetization dynamics experiments are carried out in a home-built vector network analyzer ferromagnetic resonance (VNA FMR) spectrometer with a maximum magnetic field of 6 kOe and frequencies spanning from 2 to 26 GHz using a broadband coplanar waveguide. We use a spring-loaded sample holder to improve the FMR signal-to-noise ratio, the details of which are described in a previous report [30].

First-principles calculations of the spin-resolved density of states (DOS) are implemented using the Vienna *ab initio* simulation package (VASP). The stacked structures are relaxed with Monkhorst-Pack k mesh of $15 \times 15 \times 1$ and the force criteria of 1 meV/Å. Then, magnetic anisotropy energy (MAE) calculations are performed by adopting a Monkhorst-Pack k mesh of $33 \times 33 \times 1$.

The film microstructure is characterized with a Tecnai G2 F20 transmission electron microscope (TEM). The samples for TEM are prepared using a FEI DA300 focused ion beam (FIB). The 2D elemental composition is mapped by energy-dispersive x-ray spectroscopy (EDX) in drift correction mode.

III. RESULTS AND DISCUSSIONS

A. Perpendicular magnetic anisotropy

Figure 1(a) shows a typical cross-section high-resolution (HR) TEM image of annealed $Hf(5)/Co_{20}Fe_{60}B_{20}(1.11)/MgO(2)$ films. Clear stacking-crystal structures of different layers including the underlying seed layers can be observed. The nanobeam diffraction pattern from the Hf layer verifies the crystallization of the layer. While a sharp Hf/Ru interface is visible, the $Hf/Co_{20}Fe_{60}B_{20}$ interface does not appear to be as sharp. Since the thicknesses of the $Co_{20}Fe_{60}B_{20}$ layers in our stacks are approximately 1 nm, we are not able to determine the crystallinity of the ferromagnetic layer. Figure 1(b) shows individual elemental-EDX maps revealing the distributions of Hf, Fe, and Co, along with the corresponding high-angle annular dark-field scanning TEM (HAADF STEM) image.

Magnetometry measurements are performed in both out-of-plane (OP) and in-plane (IP) configurations as shown by the representative normalized M-H loops for PMA $Hf/Co_{20}Fe_{60}B_{20}(1.11)/MgO$ in Fig. 1(c). Previous reports on $NM/Co_xFe_{80-x}B_{20}/MgO$ structures have indicated the presence of a dead layer at the $NM/Co_xFe_{80-x}B_{20}$ interface and suggested interfacial diffusion as the probable origin [31–33]. For dead-layer determination, we plot magnetic moment per unit area at saturation, M_{sheet}, as a function of t_{CFB} [Fig. 1(d)]. On extrapolating the linear fit of M_{sheet} vs t_{CFB}, the dead layer in the system is estimated at approximately 0.54 nm. The EDX map of our $Hf/Co_{20}Fe_{60}B_{20}/MgO$ stack indicates possible atomic interdiffusion at the $Hf/Co_{20}Fe_{60}B_{20}$ interface, consistent with the presence of a dead layer. It is important to mention here that the dead layer is reported to be strongly influenced by the precise film-preparation method [1,34]. The effective thickness (t_{eff}), discussed in the following paragraphs, is determined by subtracting the dead-layer thickness.

Next, we determine the effective magnetic anisotropy, K_{eff}, of the films using the following relation [35,36]

$$K_{eff} = M_S \left[\int_0^1 H_\perp(m_\perp) dm_\perp - \int_0^1 H_\parallel(m_\parallel) dm_\parallel \right], \quad (1)$$

where M_S is the saturation magnetization and $H_\perp$ and $H_\parallel$ are external magnetic fields applied OP and IP, respectively. Correspondingly, $m_\perp$ and $m_\parallel$ are the normalized values of magnetizations in OP and IP, respectively. The

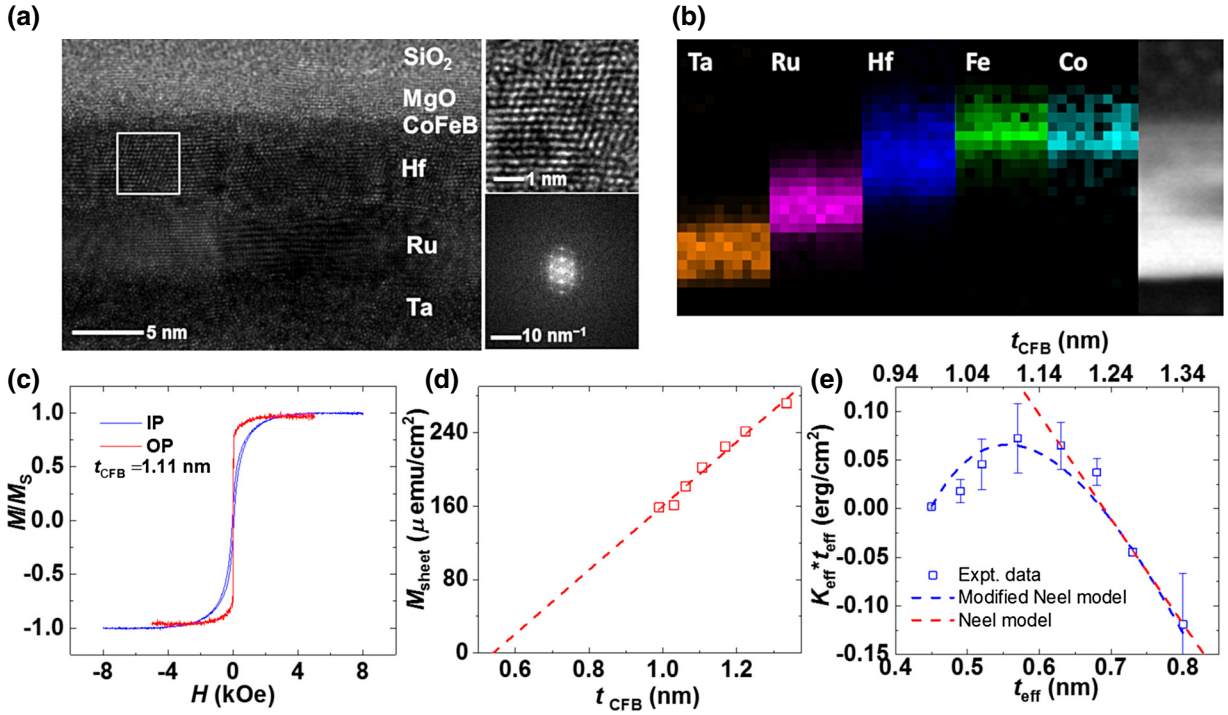

FIG. 1. (a) Cross-section HR TEM image of Hf (5)/ $Co_{20}Fe_{60}B_{20}$ (1.11)/MgO (2) film. Also shown on the right panel is the close-up TEM image and nanobeam diffraction pattern of the selected square region. (b) Individual element slices from an EDX map corresponding to the HAADF STEM image on the right for the same film. (c) M-H curve taken in IP and OP configurations of a representative $Hf/Co_{20}Fe_{60}B_{20}/MgO$ sample at $t_{CFB} \approx 1.11$ nm. (d) Plot of the magnetic moment sheet density, M_{sheet} vs t_{CFB}. The intercept of the linear fit (red dashed line) is used to determine the dead layer approximately equal to 0.54 nm. (e) Total effective anisotropy energy per unit area $K_{eff}t_{eff}$ vs t_{eff} and t_{CFB}. The red dashed line shows fitting using the Néel model, while the blue dashed line is fitting to a model which includes an additional thickness-dependent term.

expression on the right side of Eq. (1) is numerically equivalent to the area between the OP and IP magnetization loops. Figure 1(e) shows the plot of effective magnetic anisotropy per unit area, $K_{eff}t_{eff}$, as a function of t_{eff}. In order to account for the volume (K_V) and surface (K_S) contributions to the total magnetic anisotropy, we first attempt to fit the data using the Néel model as shown by the red dashed line in Fig. 1(e). The model is fitted as described by [37]

$$K_{eff}t_{eff} = K_S - (2\pi M_S^2 - K_V)t_{eff}. \tag{2}$$

The parameters as determined from fitting the Néel model are $K_S = 0.9 \pm 0.11$ erg/cm^2 and $K_V - 2\pi M_S^2 = -(1.1 \pm 0.21) \times 10^7$ erg/cm^3. We find that the value of interfacial magnetic anisotropy, which comes from the surface contributions, K_S in our Hf-underlayer films, is slightly lower than its previously reported value [13]. This is likely due to the strong nonlinearity in the $K_{eff}t_{eff}$ vs t_{eff} particularly for $t_{eff} < 0.6$ nm, which deviates from the simple Néel model, resulting in the underestimation of K_S in this system. On the other hand, if we use the modified equation proposed by Gowtham *et al.*, as shown by the blue dashed line in Fig. 1(e), we can fit the entire range of t_{eff} [34]. The equation for this model is

$$K_{eff}t_{eff} = K_S - (2\pi M_S^2 - K_V)t_{eff} + \frac{K_3}{t_{eff}}, \tag{3}$$

where K_3 is a constant so that the last term in Eq. (3) gives a contribution to K_{eff} that scales with $1/t_{eff}^2$. Our fitting results yield $K_S = (3 \pm 0.63)$ erg/cm^2, $K_V - 2\pi M_S^2 = -(2.6 \pm 0.54) \times 10^7$ erg/cm^3, and $K_3 = -(8 \pm 1.76) \times 10^{-8}$ erg/cm. The strength of the last term that includes K_3 becomes significant for $t_{CFB} < 1.3$ nm, and hence it is essential to consider this effect to obtain an accurate value of K_S. The nonlinearity of $K_{eff}t_{eff}$ in ultrathin $Ta/Co_xFe_{80-x}B_{20}/MgO$ films has been attributed to interfacial magnetoelasticity [36]. For ultrathin ferromagnets, where the surface-to-volume ratio is relatively large, it has been argued that the interfacial or surface magnetoelasticity becomes significant [38,39]. The nonlinear curves of $K_{eff}t_{eff}$ vs t_{eff} have been reported not just in $Co_xFe_{80-x}B_{20}$-based heterostructures, but also in magnetic multilayers such as Co/Au [12,34,35,40]. However, in Co/Au multilayers, this effect is attributed to coarsening of the Co-Au interfaces [40]. At such ultrathin limits, where interfaces are not ideal, it is difficult to separate the various effects

contributing to the $1/t_{\text{eff}}^2$ term. Nonetheless, our calculated value of K_S from Eq. (3) is expected to be more accurate and is supported by first-principles calculations as discussed below.

By considering spin-orbit coupling in first-principles calculations, we look at the effect of orbitals and elemental intermixing on this system. We determine the magnetic anisotropy energy (MAE), using second-order perturbation theory, for the model Hf(5 ML)/Co-Fe(7 ML = 0.84 nm)/MgO(3 ML), where ML represents monolayers. The calculation determines the MAE or K_S to be 2.92 erg/cm^2 for the Hf-underlayer system, which is identical to our experimental values. In the MAE calculation, there are two important factors —(i) the spin-orbit interaction parameter ($\xi = 0.72$ eV) and (ii) the coupling strength between the occupied and unoccupied d orbitals. The calculations show strong coupling between the occupied and unoccupied states of d_{xz} and d_{yz} orbitals, which are the major contributors to MAE, whereas in d_{xy}, $d_{x^2-y^2}$, and d_{z^2} orbitals the coupling is weaker [41]. Further calculations show that the number of Co-Fe ML does not significantly alter K_S. Also, elemental intermixing as large as 50% of interfacial atomic sites replacement does not lower the interfacial PMA of the system [41]. Since K_S is unlikely to be altered by a partly intermixed interface, it is reasonable that our experimental value of K_S would be similar to that of an ideal Hf/Co-Fe/MgO system.

B. Gilbert damping and spin pumping

In this section, we focus on magnetization dynamics study for the set of Hf/$Co_{20}Fe_{60}B_{20}$(1–1.3 nm)/MgO films that can be potentially adopted in a MRAM-free layer. In field-sweep measurements, the FMR spectra are recorded by keeping the microwave frequency and power constant while sweeping the externally applied magnetic field in the OP direction. A typical measurement set of the VNA transmission parameter $S_{12}(H)$, for a sample with $t_{\text{CFB}} \approx 1.25$ nm, taken in OP field-sweep mode at select frequencies is shown in Fig. 2(a). The FMR absorption peaks can be well fitted by the combined Lorentz absorption and dispersion line shapes which follow the equation [42,43]

$$S_{12} = \frac{A\Delta H^2}{[(H - H_{\text{res}})^2 + \Delta H^2)]} + \frac{B\Delta H(H - H_{\text{res}})}{[(H - H_{\text{res}})^2 + \Delta H^2)]} + C, \quad (4)$$

where H_{res} is the peak resonance field, ΔH is the full width at half maximum (FWHM), A and B are coefficients, and C represents the spectral background.

The resonance fields, H_{res}, at the subsequently applied microwave frequencies are summarized and plotted in Fig. 2(b) for select $t_{\text{CFB}} \approx 1.1$, 1.17, 1.23, and 1.25 nm. The resonance condition in the OP configuration can be fitted by the well-known Kittel equation in OP configuration, which is described as follows [44]:

$$f = \frac{|\gamma|}{2\pi}(H_{\text{res}} - M_{\text{eff}}), \quad (5)$$

where $|\gamma| = g_\perp \mu_B/\hbar$ is the gyromagnetic ratio, $g_\perp$ is the spectroscopic splitting factor as determined from fitting the OP FMR data, μ_B is the Bohr magneton, and M_{eff} is the effective magnetization. Figure 2(c) shows the plot of resonance linewidth as a function of frequency for the same set of t_{CFB}. The measured effective damping parameter (α_{eff}) is determined from the fit of Fig. 2(c), according to the equation [30,45,46]

$$\Delta H = \frac{4\pi\alpha_{\text{eff}}}{|\gamma|} f + \Delta H_0, \quad (6)$$

where ΔH_0 represents the inhomogeneous linewidth broadening. The value of $|\gamma|$ is determined from Eq. (5), and is subsequently used as a known parameter in fitting the data in Fig. 2(c). The measured effective damping as a function of film thickness is plotted in Fig. 2(d). α_{eff} shows a strong dependence on t_{CFB} varying from approximately 0.026 to approximately 0.011 within the range of our thickness consideration. This strong dependence of α_{eff} on ferromagnetic thickness primarily comes from nonlocal or extrinsic contributions to the measured damping, which will be discussed in the following sections. A relevant comparison of damping in the PMA region can be made with the popular Ta underlayer in order to assess the suitability of Ta replacement with Hf in the MRAM free layer. The damping in PMA Ta/CoFeB/MgO is reported as approximately 0.015, while in PMA Hf/$Co_{20}Fe_{60}B_{20}$/MgO, it can reach as low as approximately 0.012 ± 0.004 [47–49]. Hence, from our magnetometry and FMR studies, we can conclude that Hf/$Co_{20}Fe_{60}B_{20}$/MgO can provide improvements in both K_{eff} and α for PMTJs over their Ta-based counterparts.

The total measured damping of the Hf underlayer samples, measured in OP configuration, can be reduced to [49]

$$\alpha_{\text{eff}} = \alpha_{\text{int}} + \alpha_{\text{rad}} + \alpha_{\text{sp}}, \quad (7)$$

where α_{int} is the intrinsic value of damping, α_{rad} is the contribution from inductive coupling of the precessing magnetization and the coplanar waveguide, and α_{sp} represents spin pumping into the adjacent Hf layer. For simplicity in comparison, we would use α_{int} as the damping intrinsic to the heterostructure rather than intrinsic to the ferromagnet unless otherwise mentioned. α_{int} is the term that is dependent on the itinerant electrons and unlike α_{sp} does not depend on the thickness of the spin-sink layer [51]. The thickness-dependent enhancement of measured damping

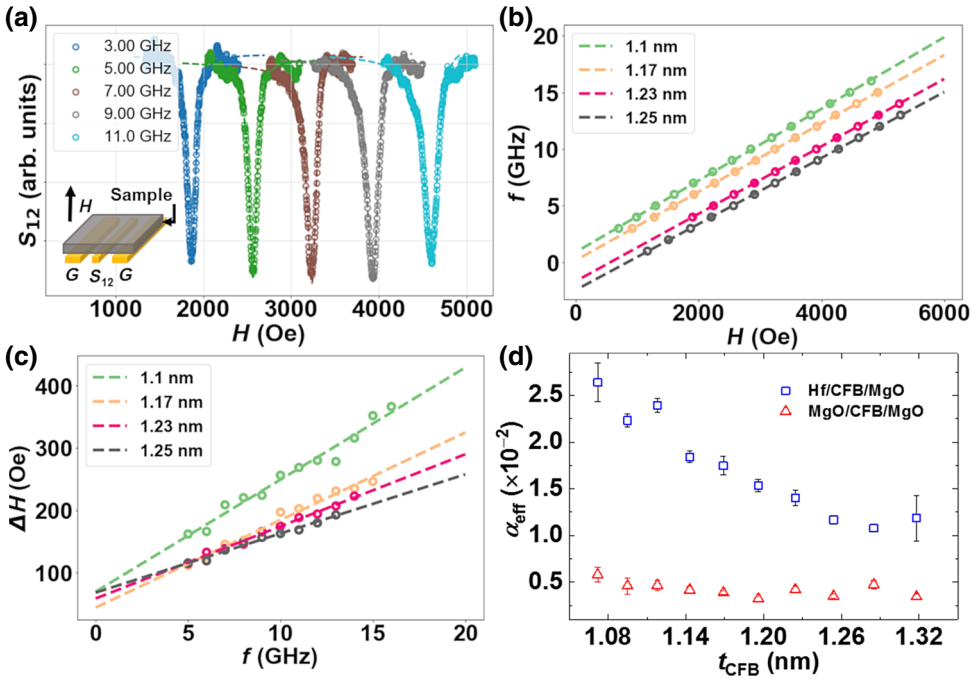

FIG. 2. (a) FMR spectrum for $Hf/Co_{20}Fe_{60}B_{20}/MgO$ for $t_{CFB} \approx 1.25$ nm, measured in OP field-sweep mode at various frequencies. Inset is the schematic of the OP field-sweep FMR measurement. (b) Frequency vs resonance field for $Hf/Co_{20}Fe_{60}B_{20}/MgO$ at select $Co_{20}Fe_{60}B_{20}$ thicknesses. The dashed line represents the fitting to the Kittel equation. (c) Linewidth vs frequency for the same set of $Hf/Co_{20}Fe_{60}B_{20}/MgO$ samples fitted using Eq. (6). (d) Measured damping as a function of t_{CFB}, determined from the fitting shown in (c), is plotted for both $Hf/Co_{20}Fe_{60}B_{20}/MgO$ (square symbols) and $MgO/Co_{20}Fe_{60}B_{20}/MgO$ (triangular symbols).

is more likely to come from spin-pumping contributions. We first look into the role of spin pumping by choosing the $MgO/Co_{20}Fe_{60}B_{20}/MgO$ (double-MgO) system, a system with suppressed spin pumping, as a reference sample [52]. The difference ($\Delta\alpha = \alpha_{sample} - \alpha_{reference}$) in measured damping, at the same t_{CFB}, accounts for contributions from α_{rad} and α_{int}. Here, our working hypothesis is $\Delta\alpha \approx \alpha_{sp}$, assuming $\alpha_{int}(\text{sample}) \approx \alpha_{int}(\text{reference})$. Figure 3(a) shows the plot of $\Delta\alpha$ vs $1/t_{CFB}$ along with a linear fit (dashed line), which shows reasonable linearity.

$MgO/Co_{20}Fe_{60}B_{20}/MgO$ structures, besides suppressing spin pumping, also prefer bcc (001) crystallinity [52]. While selecting our reference film, we make sure that its magnetic parameters including damping are minimally influenced by the MgO thickness or the capping layer. Cap materials, such as Ta on double-MgO films, can strongly influence the damping values [53]. In comparison, we find that choosing $SiO_2(8)$ as the cap yields considerably lower damping at a similar $Co_{20}Fe_{60}B_{20}$ thickness.

The spin-pumping component, $\Delta\alpha$, originating from the $Hf/Co_{20}Fe_{60}B_{20}$ interface can be expressed as [54–56]

$$\Delta\alpha \approx \alpha_{sp} = \frac{|\gamma|\hbar}{4\pi M_S t_{CFB}} g_{eff}^{\uparrow\downarrow}, \tag{8}$$

where $g_{eff}^{\uparrow\downarrow}$ is the effective spin-mixing conductance. This parameter represents the flux of spin angular momentum flowing through the $Hf/Co_{20}Fe_{60}B_{20}$ interface as a result of time-varying magnetization dynamics of the ferromagnet [56–58]. By using the values of $|\gamma|$ determined from FMR and M_S determined from magnetometry at each t_{CFB}, we compute the values of $g_{eff}^{\uparrow\downarrow}$ at each t_{CFB} using Eq. (8) and plot the results in Fig. 3(b). We can see that the values of $g_{eff}^{\uparrow\downarrow}$ cluster around $(1–2) \times 10^{20}$ m^{-2} and do not show dependence on t_{CFB}. Comparing with previously reported values of spin-mixing conductance, a strong spin-pumping interface such as Co/Pt exhibits 1×10^{20} m^{-2} while a weak spin-pumping system such as $Co_xFe_{80-x}B_{20}/Cu/Pt$ yields $(0.07–0.09) \times 10^{20}$ m^{-2} [50,59]. It has been suggested that the $g_{eff}^{\uparrow\downarrow}$ of a ferromagnetic conductor–normal metal interface is mainly determined by the normal metal [60]. Hence, we can interpret that the dominant mechanism of Gilbert-damping enhancement in our system originates from the large spin-mixing conductance at the $Hf/Co_{20}Fe_{60}B_{20}$ interface.

Finally, effective damping may have contributions from two-magnon scattering [61–63]. However, this type of contribution is more pronounced for IP field measurements, while for OP measurements, it is negligible [47,63]. Therefore, for our damping values discussed so far, we can disregard its effect. In order to qualitatively compare two-magnon scattering contributions in both reference and sample, we also perform IP FMR measurements. We observe that two-magnon scattering in $MgO/Co_{20}Fe_{60}B_{20}/MgO$ is more prominent than in $Hf/Co_{20}Fe_{60}B_{20}/MgO$. As shown in Figs. 3(c) and 3(d), respectively, for $t_{CFB} \approx 1.1$ nm, there is a substantial difference in measured linewidths between OP and IP measurements for $MgO/Co_{20}Fe_{60}B_{20}/MgO$, while the difference for $Hf/Co_{20}Fe_{60}B_{20}/MgO$ is minor.

C. Effect of Hf on intrinsic damping

We briefly discuss α_{int} in $Hf/Co_{20}Fe_{60}B_{20}/MgO$ in the context of first-principles calculations. The mechanism

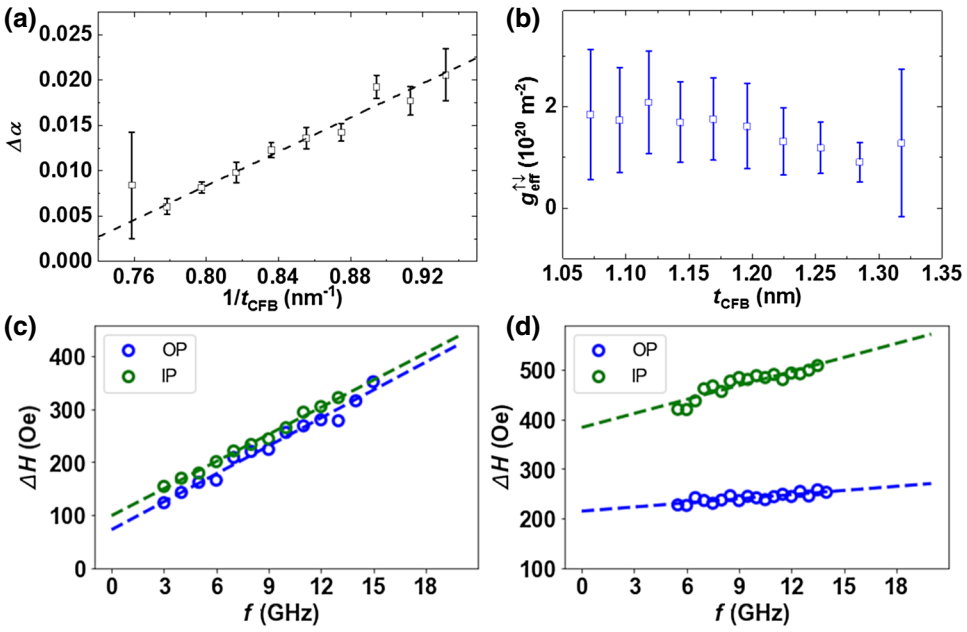

FIG. 3. (a) Plot of $\Delta\alpha$ vs $1/t_{CFB}$ along with the linear fit. In this case, $\Delta\alpha(t_{CFB}) = \alpha_{eff}$[Hf/$Co_{20}Fe_{60}/B_{20}(t_{CFB})$/MgO]– α_{eff}[MgO/$Co_{20}Fe_{60}/B_{20}(t_{CFB})$/MgO]. (b) From the slope of fitting in (a), spin-mixing conductance $g_{eff}^{\uparrow\downarrow}$ is calculated and plotted against t_{CFB}. Comparison of linewidth vs frequency data for OP and IP FMR measurements at a $Co_x Fe_{80-x}B_{20}$ thickness of approximately 1.1 nm for (c) Hf/$Co_{20}Fe_{60}/B_{20}$/MgO and (d) MgO/$Co_{20}Fe_{60}/B_{20}$/MgO.

influencing intrinsic damping is dominated by magnon-electron scattering [50]. In the previous sections, we assume that α_{int} in Hf/$Co_{20}Fe_{60}B_{20}$/MgO is identical to α_{int} in MgO/$Co_{20}Fe_{60}B_{20}$/MgO. From a materials point of view, it is interesting to compare α_{int} in these two heterostructures [50]. The intrinsic damping, α_{int}, can be characterized from the following relationship as in [64,65]

$$\alpha_{int} \sim \frac{1}{|\gamma| M_S} \mu_B^2 n(E_F) \frac{\xi^2}{W}, \tag{9}$$

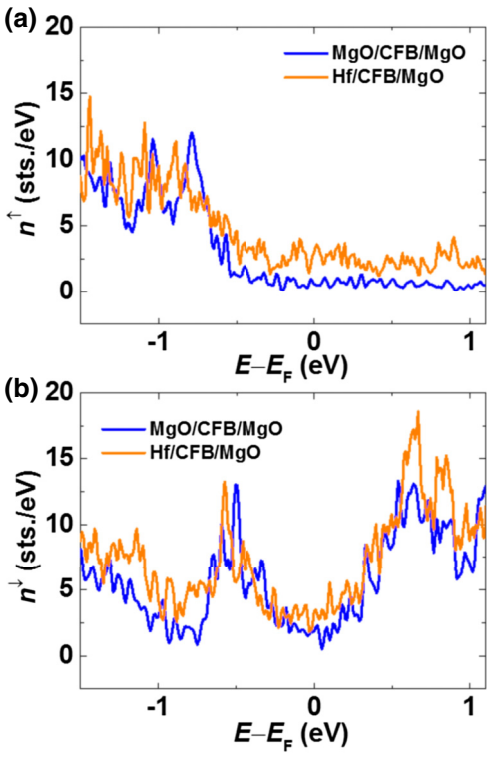

FIG. 4. Spin-resolved DOS for Hf/Co-Fe/MgO and MgO/Co-Fe/MgO. Spin channel in (a) is for the spin up while (b) is for the spin down.

where $n(E_F)$ is the total density of states (DOS) at the Fermi energy projected onto the d orbital, ξ is the spin-orbit coupling parameter, and W is the spread of DOS projected onto the d orbital in the heterostructure. For studies on systems such as $Co_{1-x}Fe_x$, the change in α_{int} is directly explained as a result of shifts in $n(E_F)$ as other parameters in Eq. (9) are assumed to remain constant within this stoichiometry variation [50,66]. In the case of heterostructures, the presence of strong spin-orbit coupling materials, such as Hf, also impacts other parameters, namely ξ and W. α_{int} in Hf/$Co_{20}Fe_{60}B_{20}$/MgO will be larger (smaller) if the product of $n(E_F)(\xi^2/W)$ is greater (lesser).

Our calculated values of $n(E_F)$, ξ, and W show that the product $n(E_F)(\xi^2/W)$ is greater for Hf/Co-Fe/MgO (Table I). Therefore, we expect the intrinsic damping of Hf-underlayer films to be larger than that of double-MgO films. Since the α_{int} of double-MgO films is expected to be closer to the intrinsic damping of bulk $Co_xFe_{80-x}B_{20}$, Hf-underlayer films will have higher α_{int} than that in bulk $Co_xFe_{80-x}B_{20}$ as well. For the sake of simplicity, first-principles calculations are done on compounds with Co and Fe at 1:1 stoichiometric ratios. Figure 4 shows the spin-resolved DOS for Hf(5 ML)/Co-Fe(7 ML)/MgO(3 ML) and MgO(3 ML)/Co-Fe(7 ML)//MgO(3 ML). Near the Fermi level, we see that DOS for the spin-up channel in Hf/$Co_{20}Fe_{60}B_{20}$/MgO is much higher compared

TABLE I. First-principles calculations of parameters determining α_{int}. $g_{\perp}$ is the spectroscopic splitting factor as determined from OP FMR measurements and is directly related to γ.

Structure	ξ(eV)	W (eV)	$n(E_F)$ (states/eV)	$g_{\perp}$
Hf/Co-Fe/MgO	0.72	12.5	9.5	2.28 ± 0.02
MgO/Co-Fe/MgO	0.016	9.1	2.6	2.1 ± 0.01

to that of $MgO/Co_{20}Fe_{60}B_{20}/MgO$, whereas for the spin-down channel, the difference is smaller. The larger α_{int} in Hf/Co-Fe/MgO is more relevant in the context of the spin-up channel. Yet, theoretical and experimental agreement on α_{int} is not perfect, and first-principles calculations predicts $\alpha_{\text{int}} \sim 0.0005$ in a clean Co-Fe system, which has not been observed experimentally [50,66,67]. Nonetheless, our calculations establish that α_{int} is larger in Hf-underlayer films.

IV. CONCLUSIONS

Our results provide comprehensive materials investigation of $Hf/Co_{20}Fe_{60}B_{20}/MgO$, and position this heterostructure to meet key MRAM requirements by investigating both PMA and damping. The true interfacial magnetic anisotropy, K_S, can be accurately determined by considering inclusion of the $1/t_{\text{eff}}^2$-dependent anisotropy term in the Néel model, and is largely unaffected by the presence of interfacial elemental intermixing. A strong thickness-dependent Gilbert damping is found for this system with spin-pumping being the primary contributor to this observed effect. Intrinsic damping and two magnon-scattering, in comparison, have smaller contributions. The spin-mixing conductance in the system is determined to be approximately 10^{20} m^{-2}, which is comparable to a ferromagnet/Pt interface. Surprisingly, even with the large spin-mixing conductance, α_{eff} can be as small as approximately 0.012 in the PMA thickness regime. The availability of a wide thickness PMA range, strong interfacial magnetic anisotropy, and large variation in damping values for PMA $Hf/Co_{20}Fe_{60}B_{20}/MgO$ opens up the degrees of freedom available for tweaking the MRAM stack for immediate applications. An important engineering follow-up work could be a Hf spacer in double-MgO free layers with the configuration $MgO/Co_{20}Fe_{60}B_{20}/Hf/Co_{20}Fe_{60}B_{20}/MgO$. This stack could provide considerable improvements in thermal stability and is expected to give higher performance than the popular Ta- or W-based counterparts.

ACKNOWLEDGMENTS

The authors would like to thank Xiuying Chen for assistance with FIB. This work was supported by the A*STAR core fund, CF-16.

[1] S. Ikeda, K. Miura, H. Yamamoto, K. Mizunuma, H. D. Gan, M. Endo, S. Kanai, J. Hayakawa, F. Matsukura, and H. Ohno, A perpendicular-anisotropy CoFeB–MgO magnetic tunnel junction, Nat. Mater. **9**, 721 (2010).

[2] D. C. Worledge, G. Hu, D. W. Abraham, J. Z. Sun, P. L. Trouilloud, J. Nowak, S. Brown, M. C. Gaidis, J. O. Sullivan, and R. P. Robertazzi, Spin torque switching of perpendicular Ta | CoFeB | MgO -based magnetic tunnel junctions, Appl. Phys. Lett. **98**, 022501 (2011).

[3] S. Yuasa, A. Fukushima, K. Yakushiji, T. Nozaki, M. Konoto, H. Maehara, H. Kubota, T. Taniguchi, H. Arai, H. Imamura, K. Ando, Y. Shiota, F. Bonell, Y. Suzuki, N. Shimomura, E. Kitagawa, J. Ito, S. Fujita, K. Abe, K. Nomura, H. Noguchi, and H. Yoda, Future prospects of MRAM technologies, IEDM 56 (2013).

[4] J. J. Nowak, R. P. Robertazzi, J. Z. Sun, G. Hu, D. W. Abraham, P. L. Trouilloud, S. Brown, M. C. Gaidis, E. J. O. Sullivan, W. J. Gallagher, and D. C. Worledge, Demonstration of ultralow bit error rates for spin-torque magnetic random-access memory with perpendicular magnetic anisotropy, IEEE Magn. Lett. **2**, 3000204 (2011).

[5] L. Thomas, G. Jan, J. Zhu, H. Liu, Y. J. Lee, S. Le, R. Y. Tong, K. Pi, Y. J. Wang, D. Shen, R. He, J. Haq, J. Teng, V. Lam, K. Huang, T. Zhong, T. Torng, and P. K. Wang, Perpendicular spin transfer torque magnetic random access memories with high spin torque efficiency and thermal stability for embedded applications (invited), J. Appl. Phys. **115**, 172615 (2014).

[6] K. Mizunuma, S. Ikeda, H. Sato, M. Yamanouchi, H. D. Gan, K. Miura, H. Yamamoto, J. Hayakawa, F. Matsukura, and H. Ohno, Tunnel magnetoresistance properties and annealing stability in perpendicular anisotropy MgO-based magnetic tunnel junctions with different stack structures, J. Appl. Phys. **109**, 07C711 (2014).

[7] M. Gottwald, J. J. Kan, K. Lee, X. Zhu, C. Park, and S. H. Kang, Scalable and thermally robust perpendicular magnetic tunnel junctions for STT-MRAM, Appl. Phys. Lett. **106**, 032413 (2015).

[8] N. Nishimura, T. Hirai, A. Koganei, T. Ikeda, K. Okano, Y. Sekiguchi, and Y. Osada, Magnetic tunnel junction device with perpendicular magnetization films for high- density magnetic random access memory, J. Appl. Phys. **91**, 5246 (2011).

[9] K. Yakushiji, T. Saruya, H. Kubota, A. Fukushima, T. Nagahama, S. Yuasa, and K. Ando, Ultrathin Co/Pt and Co/Pd superlattice films for MgO-based perpendicular magnetic tunnel junctions, Appl. Phys. Lett. **97**, 232508 (2017).

[10] J. Lourembam, B. Chen, A. Huang, S. Allauddin, and S. Ter Lim, A non-collinear double MgO based perpendicular magnetic tunnel junction, Appl. Phys. Lett. **113**, 022403 (2018).

[11] H. Almasi, D. R. Hickey, T. N.-Illige M. Xu, M. R. Rosales, S. Nahar, J. T. Held, K. A. Mkhoyan, and W. G. Wang, Enhanced tunneling magnetoresistance and perpendicular magnetic anisotropy in Mo/CoFeB/MgO magnetic tunnel junctions, Appl. Phys. Lett. **106**, 182406 (2015).

[12] G.-G. An, J.-B. Lee, S.-M. Yang, J.-H. Kim, W.-S. Chung, and J.-P. Hong, Highly stable perpendicular magnetic

anisotropies of CoFeB/MgO frames employing W buffer and capping layers, Acta Mater. **87**, 259 (2015).

[13] T. Liu, J. W. Cai, and L. Sun, Large enhanced perpendicular magnetic anisotropy in CoFeB/MgO system with the typical Ta buffer replaced by an Hf layer, AIP Adv. **2**, 032151 (2012).

[14] A. T. Hindmarch, V. Harnchana, A. S. Walton, A. P. Brown, R. M. D. Brydson, and C. H. Marrows, Zirconium as a boron sink in crystalline CoFeB/MgO/CoFeB magnetic tunnel junctions, Appl. Phys. Express **4**, 013002 (2011).

[15] X. Kozina, S. Ouardi, B. Balke, G. Stryganyuk, G. H. Fecher, C. Felser, S. Ikeda, H. Ohno, and E. Ikenaga, A nondestructive analysis of the B diffusion in Ta–CoFeB–MgO–CoFeB–Ta magnetic tunnel junctions by hard x-ray photoemission, Appl. Phys. Lett. **96**, 072105 (2010).

[16] S. Yuasa, Y. Suzuki, T. Katayama, and K. Ando, Characterization of growth and crystallization processes in CoFeB/MgO/CoFeB magnetic tunnel junction structure by reflective high-energy electron diffraction, Appl. Phys. Lett. **87**, 242503 (2005).

[17] S. S. P. Parkin, C. Kaiser, A. Panchula, P. M. Rice, B. Hughes, M. Samant, and S.-H. Yang, Giant tunnelling magnetoresistance at room temperature with MgO (100) tunnel barriers, Nat. Mater. **3**, 862 (2004).

[18] S. Yuasa, T. Nagahama, A. Fukushima, Y. Suzuki, and K. Ando, Giant room-temperature magnetoresistance in single-crystal Fe/MgO/Fe magnetic tunnel junctions, Nat. Mater. **3**, 868 (2004).

[19] W. H. Butler, X.-G. Zhang, T. C. Schulthess, and J. M. MacLaren, Spin-dependent tunneling conductance of Fe|MgO|Fe sandwiches, Phys. Rev. B **63**, 054416 (2001).

[20] Y.-W. Oh, K.-D. Lee, J.-R. Jeong, and B.-G. Park, Interfacial perpendicular magnetic anisotropy in CoFeB/MgO structure with various underlayers, J. Appl. Phys. **115**, 17C724 (2014).

[21] T. Liu, Y. Zhang, J. W. Cai, and H. Y. Pan, Thermally robust Mo/CoFeB/MgO magnetic anisotropy, Sci. Rep. **4**, 5895 (2014).

[22] J. H. Jung, S. H. Lim, and S. R. Lee, Strong perpendicular magnetic anisotropy in thick CoFeB films sandwiched by Pd and MgO layers, Appl. Phys. Lett. **96**, 042503 (2013).

[23] W.-G. Wang, M. Li, S. Hageman, and C. L. Chien, Electric-field-assisted switching in magnetic tunnel junctions, Nat. Mater. **11**, 64 (2011).

[24] K. L. Wang, J. G. Alzate, and P. Khalili Amiri, Low-power non-volatile spintronic memory: STT-RAM and beyond, J. Phys. D Appl. Phys. **46**, 074003 (2013).

[25] P. V. Ong, N. Kioussis, D. Odkhuu, P. Khalili Amiri, K. L. Wang, and G. P. Carman, Giant voltage modulation of magnetic anisotropy in strained heavy metal/magnet/insulator heterostructures, Phys. Rev. B **92**, 020407(R) (2015).

[26] W. Skowronski, T. Nozaki, D. D. Lam, Y. Shiota, K. Yakushiji, H. Kubota, A. Fukushima, S. Yuasa, and Y. Suzuki, Underlayer material influence on electric-field controlled perpendicular magnetic anisotropy in CoFeB/MgO magnetic tunnel junctions, Phys. Rev. B **91**, 184410 (2015).

[27] S. Fukami, T. Anekawa, C. Zhang, and H. Ohno, A spin-orbit torque switching scheme with collinear magnetic easy axis and current configuration, Nat. Nanotechnol. **11**, 621 (2016).

[28] M. Cubukcu, O. Boulle, M. Drouard, K. Garello, C. O. Avci, I. M. Miron, J. Langer, B. Ocker, P. Gambardella, and G. Gaudin, Spin-orbit torque magnetization switching of a three-terminal perpendicular magnetic tunnel junction, Appl. Phys. Lett. **104**, 042406 (2014).

[29] J. Lourembam, J. Huang, S. Ter Lim, and E. F. Gerard, Role of CoFeB thickness in electric field controlled sub-100 nm sized magnetic tunnel junctions, AIP Adv. **8**, 055915 (2018).

[30] S. He and C. Panagopoulos, A broadband ferromagnetic resonance dipper probe for magnetic damping measurements from 4.2 K to 300 K, Rev. Sci. Instrum. **87**, 043110 (2016).

[31] M. Yamanouchi, R. Koizumi, S. Ikeda, H. Sato, K. Mizunuma, K. Miura, H. D. Gan, F. Matsukura, and H. Ohno, Dependence of magnetic anisotropy on MgO thickness and buffer layer in $Co_{20}Fe_{60}B_{20}$-MgO structure, J. Appl. Phys. **109**, 07C712 (2012).

[32] P. K. Amiri, Z. M. Zeng, J. Langer, H. Zhao, G. Rowlands, Y.-J. Chen, I. N. Krivorotov, J.-P. Wang, H. W. Jiang, J. A. Katine, Y. Huai, K. Galatsis, and K. L. Wang, Switching current reduction using perpendicular anisotropy in CoFeB–MgO magnetic tunnel junctions, Appl. Phys. Lett. **98**, 112507 (2012).

[33] J. Sinha, M. Hayashi, A. J. Kellock, S. Fukami, M. Yamanouchi, H. Sato, S. Ikeda, S. Mitani, S. Yang, S. S. P. Parkin, and H. Ohno, Enhanced interface perpendicular magnetic anisotropy in Ta|CoFeB|MgO using nitrogen doped Ta underlayers, Appl. Phys. Lett. **102**, 242405 (2015).

[34] P. G. Gowtham, G. M. Stiehl, D. C. Ralph, and R. A. Buhrman, Thickness-dependent magnetoelasticity and its effects on perpendicular magnetic anisotropy in Ta/CoFeB/MgO thin films, Phys. Rev. B **93**, 024404 (2016).

[35] M. T. Johnson, P. J. H. Bloemen, F. J. A. den Broeder, and J. J. de Vries, Magnetic anisotropy in metallic multilayers, Rep. Prog. Phys. **59**, 1409 (1996).

[36] R. C. O'Handley, editor, *Modern Magnetic Materials: Principles and Applications* (Wiley, New York, 2000).

[37] L. Néel, Saturation approach magnetostriction, J. Phys. Radium **15**, 376 (1954).

[38] S. W. Sun and R. C. O'Handley, Surface Magnetoelastic Coupling, Phys. Rev. Lett. **66**, 2798 (1991).

[39] G. Bochi, O. Song, and R. C. O'Handley, Surface magnetoelastic coupling coefficients of single-crystal fcc Co thin films, Phys. Rev. B **50**, 2043 (1994).

[40] F. J. A. Den Broeder, D. Kuiper, A. P. Van De Mosselaer, and W. Hoving, Perpendicular Magnetic Anisotropy of Co-Au Multilayers Induced by Interface Sharpening, Phys. Rev. Lett. **60**, 2769 (1988).

[41] See supplementary materials at http://link.aps.org/supplemental/10.1103/PhysRevApplied.10.044057 for more details on first-principles calculations, magnetometry and FMR fitting.

[42] P. Durrenfeld, F. Gerhard, J. Chico, R. K. Dumas, M. Ranjbar, A. Bergman, L. Bergqvist, A. Delin, C. Gould, L. W. Molenkamp, and J. Akerman, Tunable damping , saturation magnetization, and exchange stiffness of half-heusler NiMnSb thin films, Phys. Rev. B **92**, 214424 (2015).

[43] N. Mecking, Y. S. Gui, and C.-M. Hu, Microwave photovoltage and photoresistance effects in ferromagnetic microstrips, Phys. Rev. B **76**, 224430 (2007).

[44] C. Kittel, On the theory of ferromagnetic resonance absorption, Phys. Rev. **73**, 155 (1948).

[45] Z. Celinski and B. Heinrich, Ferromagnetic resonance linewidth of Fe ultrathin films grown on a bcc Cu substrate, J. Appl. Phys. **70**, 5935 (1991).

[46] J. M. Shaw, H. T. Nembach, and T. J. Silva, Roughness induced magnetic inhomogeneity in Co/Ni multilayers: Ferromagnetic resonance and switching properties in nanostructures, J. Appl. Phys. **108**, 093922 (2010).

[47] X. Liu, W. Zhang, M. J. Carter, and G. Xiao, Ferromagnetic resonance and damping properties of CoFeB thin films as free layers in MgO-based magnetic tunnel junctions, J. Appl. Phys. **110**, 033910 (2011).

[48] N. Sato, K. P. O. Brien, K. Millard, B. Doyle, and K. Oguz, Investigation of extrinsic damping caused by magnetic dead layer in Ta-CoFeB-MgO multilayers with perpendicular anisotropy, J. Appl. Phys. **119**, 093902 (2016).

[49] T. Devolder, P.-H. Ducrot, J.-P. Adam, I. Barisic, N. Vernier, J.-V. Kim, B. Ockert, and D. Ravelosona, Damping of $Co_xFe_{80-x}B_{20}$ ultrathin films with perpendicular magnetic anisotropy, Appl. Phys. Lett. **102**, 022407 (2013).

[50] M. A. W. Schoen, D. Thonig, M. L. Schneider, T. J. Silva, H. T. Nembach, O. Eriksson, O. Karis, and J. M. Shaw, Ultra-low magnetic damping of a metallic ferromagnet, Nat. Phys. **12**, 839 (2016).

[51] M. Caminale, A. Ghosh, S. Auffret, U. Ebels, K. Ollefs, F. Wilhelm, A. Rogalev, and W. E. Bailey, Spin pumping damping and magnetic proximity effect in Pd and Pt spin-sink layers, Phys. Rev. B **94**, 014414 (2016).

[52] O. Mosendz, J. E. Pearson, F. Y. Fradin, S. D. Bader, and A. Hoffmann, Suppression of spin-pumping by a MgO tunnel-barrier, Appl. Phys. Lett. **96**, 022502 (2010).

[53] M. P. R. Sabino, S. Ter Lim, S. K. Wong, S. Ng, and M. Tran, Non-proportionality of magnetic anisotropy and damping in CoFeB/MgO-based systems, Appl. Phys. Lett. **107**, 012405 (2015).

[54] Y. Tserkovnyak, A. Brataas, G. E. W. Bauer, and B. I. Halperin, Nonlocal magnetization dynamics in ferromagnetic heterostructures, Rev. Mod. Phys. **77**, 1375 (2005).

[55] O. Mosendz, V. Vlaminck, J. E. Pearson, F. Y. Fradin, G. E. W. Bauer, S. D. Bader, and A. Hoffmann, Detection and quantification of inverse spin Hall effect from spin pumping in permalloy/normal metal bilayers, Phys. Rev. B **82**, 214403 (2010).

[56] J. M. Shaw, H. T. Nembach, and T. J. Silva, Determination of spin pumping as a source of linewidth in sputtered $Co_{90}Fe_{10}$/Pd multilayers by use of broadband ferromagnetic resonance spectroscopy, Phys. Rev. B **85**, 054412 (2012).

[57] Y. Tserkovnyak and A. Brataas, Enhanced Gilbert Damping in Thin Ferromagnetic Films, Phys. Rev. Lett. **88**, 117601 (2002).

[58] M. Zwierzycki, Y. Tserkovnyak, P. J. Kelly, A. Brataas, and G. E. W. Bauer, First-principles study of magnetization relaxation enhancement and spin transfer in thin magnetic film, Phys. Rev. B **71**, 064420 (2005).

[59] A. Ghosh, J. F. Sierra, S. Auffret, U. Ebels, and W. E. Bailey, Dependence of nonlocal gilbert damping on the ferromagnetic layer type in ferromagnet/Cu/Pt heterostructures, Appl. Phys. Lett. **998**, 052508 (2011).

[60] F. D. Czeschka, L. Dreher, M. S. Brandt, M. Weiler, M. Althammer, I.-M. Imort, G. Reiss, A. Thomas, W. Schoch, W. Limmer, H. Huebl, R. Gross, and S. T. B. Goennenwein, Scaling Behavior of the Spin Pumping Effect in Ferromagnet-Platinum Bilayers, Phys. Rev. Lett. **107**, 046601 (2011).

[61] R. Arias and D. L. Mills, Extrinsic contributions to the ferromagnetic resonance response of ultrathin films, J. Appl. Phys. **87**, 5455 (2000).

[62] J. Lindner, K. Lenz, E. Kosubek, K. Baberschke, D. Spoddig, R. Meckenstock, J. Pelzl, Z. Frait, and D. L. Mills, Non-gilbert-type damping of the magnetic relaxation in ultrathin ferromagnets: Importance of magnon-magnon scattering, Phys. Rev. B **68**, 060102(R) (2003).

[63] M. J. Hurben and C. E. Patton, Theory of two magnon scattering microwave relaxation and ferromagnetic resonance linewidth in magnetic thin films, J. Appl. Phys. **83**, 4344 (2017).

[64] B. Zhang, A. Cao, J. Qiao, M. Tang, K. Cao, X. Zhao, S. Eimer, Z. Si, N. Lei, Z. Wang, X. Lin, Z. Zhang, M. Wu, and W. Zhao, Influence of heavy metal materials on magnetic properties of Pt/Co/heavy metal tri-layered structures, Appl. Phys. Lett. **110**, 012405 (2017).

[65] V. Kamberský, On the landau–lifshitz relaxation in ferromagnetic metals, Can. J. Phys. **48**, 2906 (1970).

[66] S. Mankovsky, D. Kodderitzsch, G. Woltersdorf, and H. Ebert, First-principles calculation of the Gilbert damping parameter via the linear response formalism with application to magnetic transition metals and alloys, Phys. Rev. B **87**, 014430 (2013).

[67] A. J. Lee, J. T. Brangham, Y. Cheng, S. P. White, W. T. Ruane, B. D. Esser, D. W. McComb, P. C. Hammel, and F. Yang, Metallic ferromagnetic films with magnetic damping under 1.4×10^{-3}, Nat. Commun. **8**, 234 (2017).